Chem Catalysis

Article

Pressure-pulsed flow triples mass transport in aqueous CO_2 electrolysis

Graphical abstract

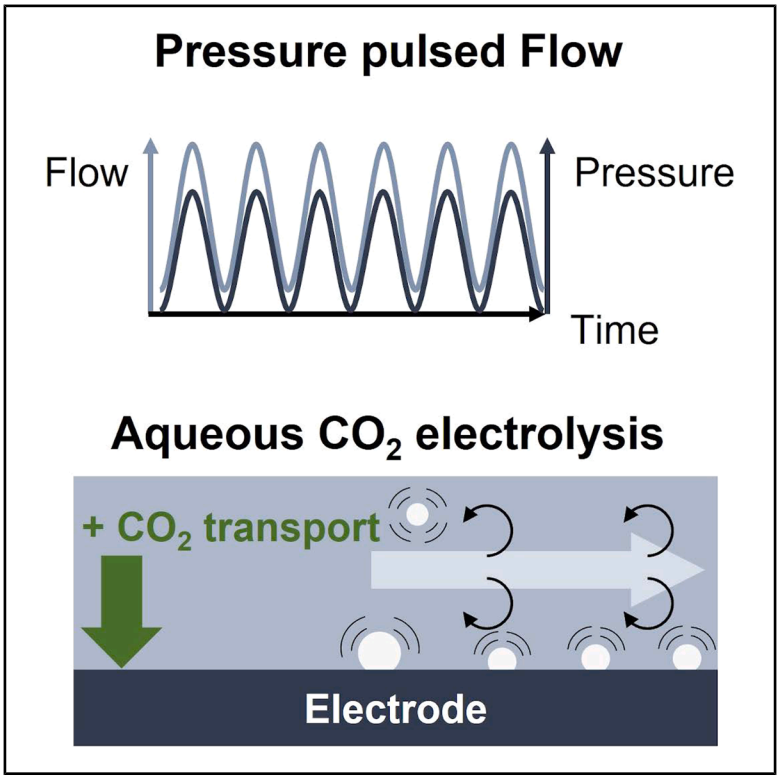

Highlights

- Aqueous CO_2R assisted by a pressure-pulsed flow (50 Hz, between 1 and 2.5 bar)
- Current densities of 87 mA cm^{-2} toward CO equivalents without the use of a GDE
- The CO_2 mass transport is enhanced through flow oscillations and vibrating bubbles
- Even higher currents should be possible with a higher pulse frequency and amplitude

Authors

Jorrit Bleeker, Lisanne C. Bakker, Sue S.J. van Deursen, ..., Evert C. Wagner, J. Ruud van Ommen, David A. Vermaas

Correspondence

d.a.vermaas@tudelft.nl

In brief

CO_2 electrolysis in fully aqueous conditions is currently strongly limited by mass transport of CO_2. Fast pressure pulses enhance the mass transport of CO_2 substantially, reaching partial current densities >80 mA/cm^2. We find that this is due to both vibration of gas bubbles and flow oscillations.

Bleeker et al., 2026, Chem Catalysis 6, 101547
January 15, 2026
https://doi.org/10.1016/j.checat.2025.101547

CellPress

Chem Catalysis

CellPress

Article

Pressure-pulsed flow triples mass transport in aqueous CO_2 electrolysis

Jorrit Bleeker,[1] Lisanne C. Bakker,[1] Sue S.J. van Deursen,[1] Timo J.J.M. van Overveld,[1] Katie M.R. Lawrence,[2] Isabell Bagemihl,[1] Giacomo Lastrucci,[1] Duco Bosma,[1] Christiaan V. Schinkel,[1] Evert C. Wagner,[1] J. Ruud van Ommen,[1] and David A. Vermaas[1,3,*]

[1]Department of Chemical Engineering, Delft University of Technology, Van der Maasweg 9, 2629 HZ Delft, the Netherlands

[2]Process & Energy Department, Faculty of Mechanical Engineering, Delft University of Technology, Leeghwaterstraat 39, 2628 CB Delft, the Netherlands

[3]Lead contact

*Correspondence: d.a.vermaas@tudelft.nl

https://doi.org/10.1016/j.checat.2025.101547

THE BIGGER PICTURE The energy transition requires moving away from fossil fuels to renewable electricity. However, sectors such as long-distance transport and plastic manufacturing need carbon-based chemicals. These sectors are responsible for hundreds of millions tons of chemicals per year, which is equivalent to 10%–20% of CO_2 emissions. Electrochemical CO_2 reduction presents a promising alternative, enabling production using only CO_2, water, and renewable electricity. To make an impact on the climate, CO_2 electrolysis needs to be urgently developed to a scalable design.

Here, we present a potential breakthrough: a liquid aqueous CO_2 electrolyzer operating under pressure-pulsed flow, improving mass transport with a cheap vibratory pump. This method achieves current densities of 87 mA cm^{-2} (an order of magnitude higher than typical aqueous systems) while using a commercial silver gauze cathode and CO_2 saturated under 1-atm CO_2 pressure. We use high-speed imaging to predict that an aqueous liquid-fed CO_2 system can attain even higher current densities.

SUMMARY

Electrochemical CO_2 reduction (CO_2R) is a promising technology for carbon recycling and energy storage. While gas-fed CO_2R is currently the best practice because it facilitates fast mass transport, CO_2R in water offers potential advantages such as avoiding salt formation, facile water control, and easier integration with CO_2 capture. In this work, we enhance mass transport in an aqueous CO_2 electrolyzer using fast pressure pulses (50 Hz, 1.2 bar) with a vibratory pump typically found in coffee machines. We demonstrate a limiting current density of 87 mA cm^{-2} toward CO_2R products—nearly three times higher than without pulses. The current density can be further increased by leveraging the peak-to-peak pressure amplitude or pump frequency, as shown through particle image velocimetry (PIV) and an order-of-magnitude scaling analysis. Although challenges remain, such as pump energy consumption, contamination, heating, and pressure-wave damping, the pressure-pulsed concept is a promising direction for aqueous CO_2R.

INTRODUCTION

The electrochemical reduction of CO_2 (CO_2R) is a promising technology that uses renewable electricity to convert CO_2 and water into fuels and chemicals, enabling carbon recycling, energy storage, and climate-change mitigation.[1–3] In CO_2R, CO_2 is converted at the cathode into products such as CO, C_2H_4, and formic acid.[4] Hydrogen is an undesirable by-product, and its reaction rate increases when the mass transport of CO_2 to the electrode is insufficient[5,6] or the catalyst is contaminated.[7,8]

To achieve higher current densities, attention has shifted toward gas-fed reactors with gas-diffusion electrodes (GDEs) and membrane electrode assemblies (MEAs).[3,9–12] With these technical features, CO_2R can reach and sustain industrially relevant current densities (>300 mA cm^{-2}, >1,000 h) and is being scaled up in start-up companies.[13,14] However, gas-fed electrolyzers still have problems with stability,[15,16] control of water,[17,18] and salt formation.[19] In addition to the aforementioned challenges, these systems require gaseous CO_2. If the CO_2 source is an environmental capture system, such as direct air capture with alkaline[20,21] or amine solutions,[21,22] the CO_2 will need to be removed from the capture liquid (Figure 1A).[23] In this removal step, the vacuum pumps, compressors, and de-humidifiers require 10%–35% of the energy consumption

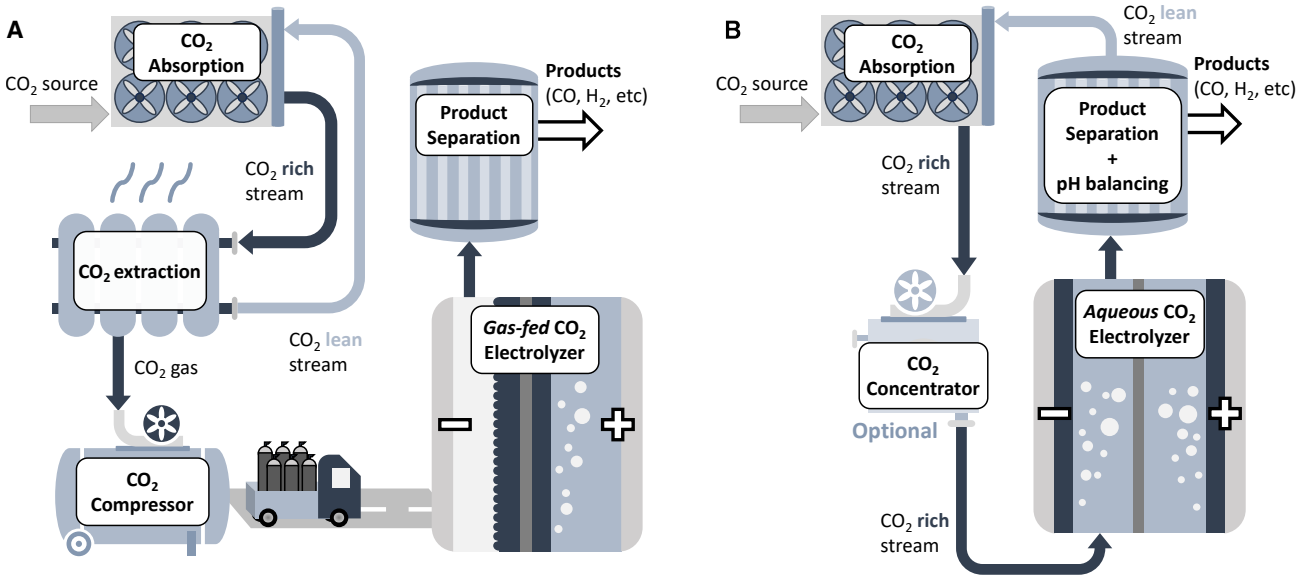

Figure 1. Process schemes for combining CO_2 capture with gas-fed and liquid-fed CO_2 electrolysis

(A) Schematic drawing of an integrated CO_2 capture-and-conversion process with a gas-fed electrolyzer.

(B) Schematic drawing of an integrated CO_2 capture-and-conversion system with an aqueous CO_2 electrolyzer. A dissolved inorganic carbon (DIC) balancing step may be required to convert some of the CO_2-capture solution into dissolved CO_2. Additionally, a pH-balancing step might be necessary to prepare the solution for CO_2 absorption.

of a current state-of-the-art CO_2 electrolyzer[21,24] (see Figure S1 for calculation).

Aqueous CO_2R can avoid these costs by directly converting dissolved CO_2 from capture solutions, which reduces the process steps and has potential to simplify the process significantly[22] (Figure 1B). Omission of the dissolved CO_2 extraction steps results in lower required capital investments,[22] although a balancing step (e.g., by adding an acid) might still be required to create dissolved CO_2 from bicarbonates. Unfortunately, aqueous CO_2R suffers from low limiting current densities toward CO_2-based products. In typical electrolyzers, the limiting current densities are an order of magnitude lower compared to GDE-based systems (5–10 mA cm^{-2} vs. 100–400 mA cm^{-2}).[25] The low limiting current densities in aqueous CO_2R are a result of depleting CO_2 concentration at the cathode surface, which is caused by the low CO_2 solubility in water and poor mass transport in traditional H-cells and traditional flow-by cells.

Two previous strategies for increasing the limiting current density in aqueous CO_2R are increasing the CO_2 concentration (e.g., by increasing the pressure,[26–28] supersaturation of CO_2,[29] or adding amines[22,30,31] or organic electrolytes with high CO_2 solubility[32,33]) and using *in situ* conversion of bicarbonate to CO_2 (e.g., with a bipolar membrane). Despite substantial work on these approaches, the industrial goals for current density, cell voltage, faradaic efficiency (FE), scalability, and lifetime are not fully met.[34]

A complementary strategy is to leverage hydrodynamic disturbances near the electrodes. For example, nano-structured catalysts can break up the diffusion boundary layer through bubble-induced mass transport and obtain a 3-fold increase in current density compared to a flat electrode.[6,35,36] Similarly, microfluidic gas-liquid devices can create small diffusion boundary layers, which could give a 1- to 1.5-order-of-magnitude increase in current density compared to a liquid system.[37] The effectivity of reducing the diffusion boundary-layer thickness to achieve high current densities has been confirmed by Wen et al., who obtained CO_2-to-CO current densities of >1,000 mA cm^{-2} in an exsolution-induced flow cell,[38] with a calculated boundary-layer thickness of <1.5 μm. While effective, these three approaches (nano-structured catalysts, leverage of microfluidics, and exsolution-induced flow cells) require complex reactor and electrode design.

Hydrodynamic methods for reducing the boundary-layer thickness are studied more widely in other electrochemical applications. We take inspiration from operating under oscillatory flow conditions (Figure 2A), induced with a piston or pulsating pump, causing vortices in the electrolyte. The vortices create flow perpendicular to the electrode instead of mainly unidirectional flow parallel to the electrode surface.[39] Oscillatory flow has been successfully applied in electrodialysis,[40] redox flow batteries[41] and electrochemical reactors.[39,42] The oscillation frequencies applied in these studies were between 0.2 and 3 Hz and resulted in a 2×[39,40] to 5×[42] higher limiting current density compared to a steady flow.

In this work, we apply a pressure-pulsed flow to increase the limiting current density (j_{lim}) in aqueous CO_2R. Similar to an oscillatory flow, pressure-pulsed flow induces pressure fluctuations but at a higher frequency (Figure 2B). We create 50-Hz oscillations in the pressure, in which the pressure fluctuates between 1 and 2.2 bar, with a cheap (~18 euro) vibratory pump, typically used in household coffee machines. We experimentally evaluate the mass transport by measuring the limiting current

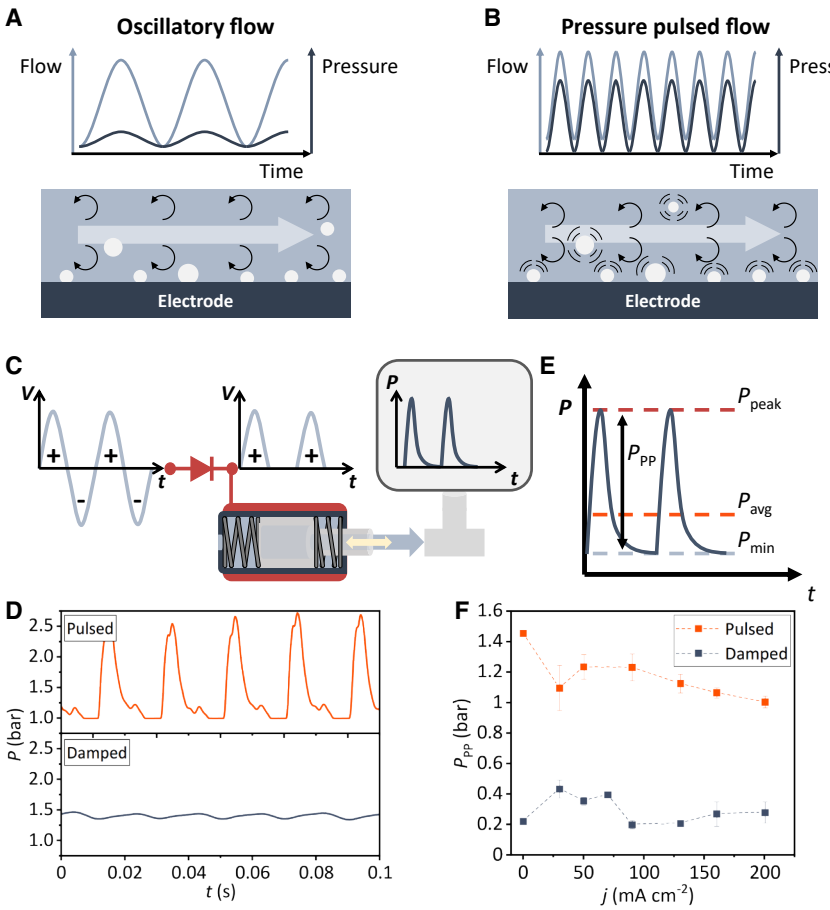

Figure 2. Mechanisms of different flow regimes and characteristics of pump pressure profiles

(A) Hypothesized mixing behavior during oscillatory flow.

(B) Hypothesized mixing behavior during pressure-pulsed flow.

(C) Diagram with the workings of a vibratory pump.

(D) Pressure waves at the inlet of the cathode channel in the electrolyzer with no applied current (pulsed) and when two pressure dampers are installed (damped).

(E) Schematic presentation of the peak pressure (P_{peak}), minimum pressure (P_{min}), time-averaged pressure (P_{avg}), and the peak-to-peak pressure (P_{PP}).

(F) P_{PP} at the inlet of the cathode for different current densities for pressure pulses and damped pulses. All experiments were performed with duplicates; error bars are the standard error.

density on a commercial silver mesh cathode and compare this to a system where pressure dampers are installed. Additionally, the mass-transport mechanisms are further studied with high-speed imaging and particle image velocimetry (PIV). Through an order-of-magnitude scaling approach, we conclude that both vibrating bubbles and multidirectional oscillatory flow contribute to enhancing the CO_2R. Finally, we evaluate the scalability of an aqueous pressure-pulsed CO_2R system and discuss three possible issues.

RESULTS

Generation and characterization of pressure-pulsed flow

To ensure adequate mass transport for aqueous CO_2R, we generate pressure pulses that oscillate the fluid and cause gas bubbles to vibrate. Our vibratory pump comprises a diode, a spool, and a magnetic piston (Figure 2C).[43] When connected to an alternating current (AC) grid (50 Hz, 220 V), the diode converts the electrical signal into a half-wave rectified sine. This creates a periodic electric field in the spool, which moves the piston. As a result, the piston generates 50 pressure pulses per second with an amplitude of 1.5 bar and a flow rate of 530 mL min^{-1} (average velocity of 8.9 mm s^{-1} in our cell).

However, the pressure waves before and after the electrolyzer were more complex than a half-wave rectified sine (Figure 2D). We hypothesize that these extra peaks in the pressure wave are not generated by the pump but instead result from reflections and vibration in the electrolyzer (see Figure S2). To understand the effects of pressure pulses on the CO_2 electrolyzer, we also created a reference case where we damped out the pressure waves with pressure dampers (Figure 2D). Here, the pressure amplitude reduced significantly, but the flow rate remained the same (see Figure S3).

To characterize the shapes and waveforms, we introduce the following parameters to describe the pressure waves (Figure 2E), which are all applied on datasets of >500 pressure waves (i.e., >10 s of data):

(1) P_{avg}: time-averaged pressure for each dataset
(2) P_{PP}: peak-to-peak pressure, $P_{peak} - P_{min}$, averaged over all pressure waves
(3) χ: relative expansion, P_{peak}/P_{min}, averaged over all pressure waves. χ expresses the ratio of volume change of gas bubbles (according to the ideal gas law) during the pressure pulse.

Figure 2F shows P_{PP} for the pressure-pulsed and damped CO_2 electrolysis experiments, averaged over four pressure sensors and 40 min of pressure data. The dampers are effective at reducing the P_{PP} by 70%–80% and will be a useful comparison case to study the effect of pressure pulses on mass transport. The difference is even larger in χ, 2–2.2 for pressure-pulsed flow and 1.2–1.3 for damped flow, while the P_{avg} is similar for both pulsed flow and damped flow (Figure S4).

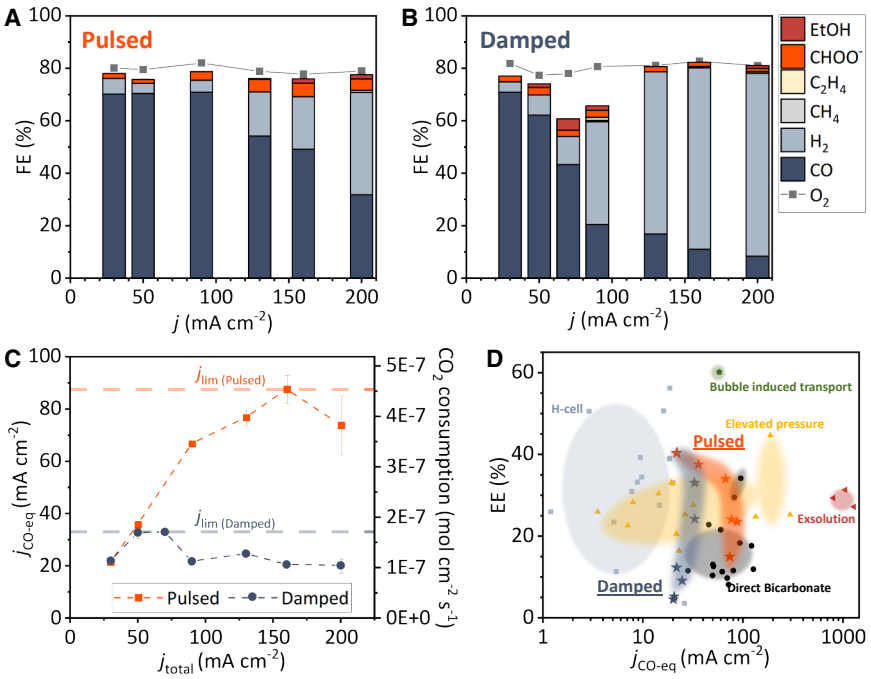

Figure 3. Performance of pressure-pulsed CO_2 electrolysis compared to damped flow and literature benchmarks

(A) FE against total current density under pressure-pulsed flow.

(B) FE against total current density under damped flow. For comparison, FE_{O2} at the anode is also shown.

(C) Partial current density as if all products were CO ($j_{CO\text{-}eq}$) against total current density, also displayed as molar CO_2 consumption on the right axis. Operating conditions: Ag mesh cathode, IrOx anode, 20°C, 0.5 M $KHCO_3$ saturated with 1 atm CO_2. All experiments were performed with duplicates; error bars are the standard error. The cathode voltage during the CO_2R experiments is shown in Figure S6.

(D) Literature comparison of energy efficiency (EE) and limiting current density ($j_{CO\text{-}eq}$). Here, we define the EE as FE × voltage efficiency. See Figure S7 for data and references.

Effect of fast pressure pulses on CO_2R performance

To express the performance of the pressure-pulsed aqueous CO_2 electrolyzer, we use the limiting current density (j_{lim})—the maximum obtained partial current density of CO_2R, at which the CO_2 concentration at the cathode surface is assumed to approach zero.

Figures 3A and 3B show the FE after 10 min of electrolysis for a pressure-pulsed and a damped system under constant current. Up to 50 mA cm^{-2}, the faradaic efficiencies are very similar for the two flow types. CO is the major product with 60%–70% FE, while less than 10% of the current is used for H_2. We note that this partial current density for CO_2R is significantly higher than most reported H-cells (Lee et al.[25] report 50+ systems with current densities below 5–10 mA cm^{-}). At higher current densities, the FE for the damped system (Figure 3B) significantly decreases, indicating strong CO_2 mass-transport limitations. At the same time, the pulsed (Figure 3A) system still performs well (FE_{CO} > 50%) at 130 mA cm^{-2}. Even at 200 mA cm^{-2}, approximately half of the observed products are CO_2R products, including small amounts (FE_i < 5%) of CH_4, C_2H_4, $CHOO^{-}$, and EtOH. We hypothesize that the non-CO products are a result of ppm-level Cu contaminations on the electrode (Figure S5).

The total FE was close to 80% at both the anode and cathode. The remaining 20% of products is lost because catholyte and anolyte are mixed in the same container. This leads to faradaic losses, as some O_2, CO_2R products, and H_2 are recycled and consumed at the electrodes instead of producing new products. We expect the actual FE toward CO_2R products to be slightly higher when catholyte and anolyte are separated.

Figure 3C compares the partial current densities of a pressure-pulsed and damped system. To express the consumption of CO_2 while taking care of the number of electrons per CO_2 molecule, we introduce the equivalent CO partial current ($j_{CO\text{-}eq}$), which is the current as if all products were CO:

$$j_{CO-eq} = j_{CO} + \frac{1}{4}j_{CH4} + \frac{1}{3}j_{C2H4} + j_{CHOO^-} + \frac{1}{3}j_{EtOH.} \quad \text{(Equation 1)}$$

Here, j_i is the current density toward a specific CO_2R product, which is multiplied with the ratio of electrons compared to CO (n_{CO}/n_i, where n is the number of electrons per molecule of product). Under pressure-pulsed flow, a maximum $j_{CO\text{-}eq}$ of 87 mA cm^{-2} is obtained, compared to 33 mA cm^{-2} when the flow is damped. Hence, the fast pressure pulses increase the limiting current density of CO_2R products by 2.6 times. Because the flow rate and P_{avg} for the flow regimes are the same, we can conclude that pressure pulses are the main cause of increased CO_2 mass transport. Additionally, as CO_2 is saturated in the electrolyte at 1 atm, increasing the pressure in the liquid during the pulses does not significantly raise the dissolved CO_2 concentration. This suggests that the performance increase is caused by dynamic replenishment of CO_2 at the catalyst surface by the pressure pulses.

A partial current density of 87 mA cm^{-2} is among the highest reported for aqueous CO_2R.[25] To compare our work to other aqueous CO_2R works, the $j_{CO\text{-}eq}$ is plotted against the energy efficiency (EE) (Figure 3D). We define EE as the product of FE and voltage efficiency.

H-cell-based systems can reach a high EE (25%–50%) but typically only reach $j_{CO\text{-}eq}$ of 5–10 mA cm^{-2}.[28,44–50] An exception to this is the work of Burdyny et al.,[6] which utilizes gold nano-structured electrodes to promote gas-bubble-induced mass transport to achieve a $j_{CO\text{-}eq}$ of ~55 mA cm^{-2}. Systems operating under higher pressures (3–10 bar)[28,29,48] could alleviate mass-transport limitations as the CO_2 solubility linearly

Table 1. Calculation of the diffusion boundary-layer thickness, δ, for different temperatures at 1 atm of CO_2 for a j_{lim} of 87 mA cm^{-2} and 33 mA cm^{-2}

T (°C)	C^*_{CO2} (mol m^{-3})	D_{CO2} (m^2 s^{-1})	δ_{Pulsed} (μm)	δ_{Damped} (μm)
15	45.6	$1.45 \cdot 10^{-9}$	14.6	38.6
20	39.2	$1.67 \cdot 10^{-9}$	14.5	38.3
25	34.1	$1.91 \cdot 10^{-9}$	14.5	38.1
30	30.0	$2.17 \cdot 10^{-9}$	14.5	38.1

Solubility and diffusion data from CRC.[55] Pulsed values, 87 mA cm^{-2}; damped values, 33 mA cm^{-2}.

increases with pressure. However, only Lamaison et al.[48] reported high partial current densities (up to 287 mA cm^{-2}) at 10 bar. A direct bicarbonate electrolysis-based system[8,51–54] can reach similar or slightly higher current densities to our system ($j_{CO\text{-}eq}$ of 45–127 mA cm^{-2}) but requires an increased voltage for the bipolar membrane. The exsolution-based system[38] remains the best of the reported aqueous CO_2R systems to date, with both high currents (~1,000 mA cm^{-2}) and a good EE. These high current densities were achieved with a flow-through electrode in combination with a CO_2 supersaturated electrolyte.

The high $j_{CO\text{-}eq}$ in the exsolution-based system was achieved when combining methods to increase the CO_2 concentration and mass transport. In that line of reasoning, pressure-pulsed CO_2 electrolysis can further expand its potential when combined with CO_2 supersaturation or pressurization and reach even higher current densities.

The mass-transport mechanisms of pressure-pulsed flow

To understand the effectivity of pressure-pulsed flow for increasing the limiting current density (j_{lim}), we estimate the diffusion boundary-layer thickness. With the assumption that the current density is only limited by mass transport of CO_2 toward the cathode, j_{lim} can be expressed as follows:

$$\frac{j_{lim}}{nF} = \frac{D_{CO2} C^*_{CO2}}{\delta}. \qquad \text{(Equation 2)}$$

Here, n is the amount of electrons per CO_2, F is the Faraday constant, D_{CO2} is the diffusion coefficient of CO_2, C^*_{CO2} is the bulk concentration of CO_2, and δ is the diffusion boundary-layer thickness. Using a j_{lim} of 87 mA cm^{-2} in Equation 2, we calculate the diffusion boundary-layer thickness to be approximately 14.5 μm. For damped pressure pulses, the estimated δ is 38 μm. The limiting current density should be relatively unaffected by the temperature changes during experiments (18°C–30°C), as the changes in D_{CO2} and C^*_{CO2} balance each other (see Table 1).

We acknowledge that our system operates at a higher flow rate than conventional CO_2 electrolyzers, but this alone cannot explain the increase in current densities (see Figure S8). We identified two other mixing mechanisms by studying the electrolyzer with high-speed imaging and PIV: the vibration of gas bubbles caused by fast pressure changes (Figure 4A) and multidirectional oscillatory flow (Figure 4D).

Vibrating gas bubbles

In the high-speed videos (see Videos S1, S2, S3, S4, and S5), we observed growing and shrinking gas bubbles on the electrode (Figure 4A). These vibrations were caused by the rapid pressure changes during a pulse (1–2.5 bar, Figure 4B). Figure 4C shows the gas bubbles at different stages of the pressure pulse, which drive fluid in all directions by growing and shrinking.[56] Notably, some gas bubbles also move inside the porous mesh electrode during the peak of the pulse, thereby pulling fluid toward the electrode. We believe these vibrations enhance the mixing of electrolyte from the bulk to the electrode, thereby sustaining high local CO_2 concentrations. The volume of the bubbles scales with pressure according to the ideal gas law:

$$\frac{V_{min}}{V_{peak}} = \frac{d^3_{min}}{d^3_{peak}} = \frac{P_{peak}}{P_{min}} = \chi. \qquad \text{(Equation 3)}$$

Here, V_i, and d_i are the bubble volume and the bubble diameter at the peak and minimum of a pressure wave. The convective mass transport around the bubbles (quantified in mass-transfer coefficient k_{Bubble}, in m s^{-1}) scales with the local velocity perpendicular to the electrode (v_x), which at the bubble-liquid interface is equal to dd/dt:

$$k_{Bubble} \propto v_{x,Bubble} \sim \frac{dd}{dt} \sim \frac{d_{peak} - d_{min}}{t_{peak}} \sim \frac{d_{min}}{0.1/f}\left(\chi^{-1/3} - 1\right). \qquad \text{(Equation 4)}$$

Here, t_{peak} is the time between a minimum and maximum pressure, which is about $0.1/f$ in our experiments, where f is the frequency of the pump in s^{-1}. Hence, when comparing two systems with gas bubbles of similar amounts and sizes, the mass transport due to oscillating bubbles scales with the ratio between $f(\chi^{-1/3}-1)$ in the pulsed flow and the damped flow.

Multidirectional oscillatory flow

The inlet of the flow channel is inclined relative to the electrode's surface (Figure 6B). This, in combination with the relatively high flow rate and oscillations, creates a complex transient flow with velocities components in all three dimensions (Figure 4D), which improves the mass transport. To gain a better understanding of the mixing behavior, the velocity field near the cathode was visualized with PIV (see Figure S9). We did not observe turbulence but rather multiple periodic circulations within the flow, which matches the regime of the time-averaged Reynolds number (Re 10–100). Figure 4E shows the v_x during a pressure pulse at 0.5 mm from the electrode(see Figure S10 for v_y). The velocity profile does not significantly change while varying the distance from the electrode (0.05, 0.1, and 0.25 mm). This indicates that the electrolyte goes through the porous electrode (Figure S10).

The mixing due to oscillatory flow scales with v_x, which we hypothesize to scale with dP/dt. This is observed in Figure 4F, where the largest peaks in pressure change (dP/dt), in the first 4 ms of the wave, have a similar profile to v_x. Our hypothesis for the relation between v_x and dP/dt is further supported by estimating the pressure gradient dP/dy due to oscillations, which is an order of magnitude larger than the pressure drop due to mean flow in our system (see

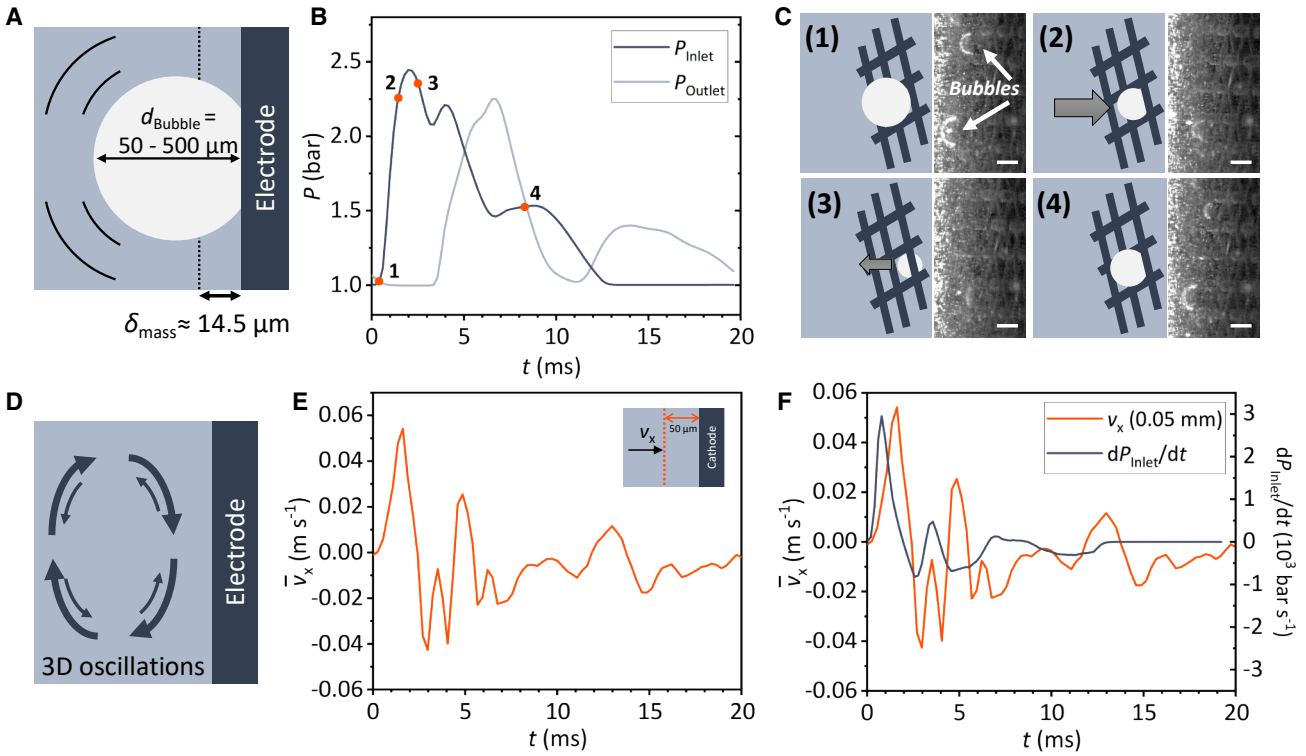

Figure 4. Mass-transport mechanisms in pressure-pulsed CO_2R

(A) Growing and shrinking gas bubbles due to the pressure changes. Typical bubble diameters (d_{bubble}) are 50–500 µm; δ_{mass} is the mass-transport boundary layer.

(B) Pressure wave during high-speed imaging averaged over 350 pulses; points correspond to images in (C).

(C) Image of the Ag mesh during a pressure pulse; a gas bubble is moving in and out of the pore. Scale bar, 200 µm.

(D) Mixing due to the multidirectional oscillatory flow and circulations.

(E) Average fluid velocity perpendicular to the electrode (v_x) at 50 µm from the electrode surface, obtained with PIV and averaged over 10 pulses. The time on the horizontal axis corresponds to that in (B). For more information, see Figure S9.

(F) Comparison of the pressure gradient measured at the inlet of the electrolyzer (dP_{Inlet}/dt) to v_x at the electrode, see Figure S10 for dP_{Outlet}/dt. See Figure S11 for PIV results of the damped case.

Figure S12 for calculation). Hence, the forces on the water due to oscillations are dominating those due to large flow rate. Using this scaling analysis, we estimate the mass transfer coefficient k_{Osc} (in m s^{-1}):

$$k_{Osc} \propto v_{x-Osc} \propto \frac{dP}{dt} \sim \frac{P_{PP}}{0.1/f}. \qquad \text{(Equation 5)}$$

The mass transport due to oscillations scales with P_{PP}, which we also observed with a statistical analysis (Figure S13). Hence, when comparing two systems, the mass transport due to oscillatory flow will scale with $f \cdot P_{PP}$ values of the two experiments.

Comparison between pulsed and damped flow

The flow properties of the pulsed and damped CO_2R experiments are compared in Table 2. The ratios of ($\chi^{-1/3}$–1) (2.2–3.9) and P_{PP} (2.5–4.5) are in the same order of magnitude as the increase in $j_{CO\text{-}eq}$ (or CO_2 mass transport toward the electrode). We conclude that both mechanisms could cause the enhanced mass transport. The exact ratio of contribution to the mass transport of these two processes will depend on the gas-bubble coverage on the electrode.

Understanding the origin of the enhanced mass transfer in pressure-pulsed flow, we can predict the conditions to further increase the limiting currents. We believe that CO_2R current densities of >100 mA cm^{-2} can be achieved if higher f, P_{PP}, and/or χ were applied in our system. At the same time, increasing f, P_{PP}, and/or χ alone would also require new equipment; our pump had limited tuning possibilities for pressure, frequency, or flow rate. We studied different vibration frequencies, but, because the flow rate and pressure amplitude strongly depend on the frequency, our pump only operates well at around 50 Hz (see Figure S16).

Considering the effectiveness of combining high CO_2 concentrations with enhanced mass transport (as shown in Figure 3D with the exsolution strategy), we highlight the potential of using elevated pressure together with high P_{PP}. An elevated pressure increases the CO_2 concentration, while a higher P_{PP} enhances the mass transfer. While χ is compromised by elevated pressure, the P_{PP} is not, thereby allowing high CO_2 concentrations and simultaneous fast mass transfer for obtaining even higher limiting current densities.

Table 2. Comparison of the scaling factors for bubble oscillation induced mixing, $\chi^{-1/3}-1$, and oscillatory flow induced mixing, P_{PP}, to the CO_2 mass transport, expressed as $j_{CO\text{-}eq}$

	$(\chi^{-1/3}-1)$ (–)	P_{PP} (bar)	$j_{CO\text{-}eq}$ (mA cm^{-2})
Pulsed flow	−0.26 to −0.30 (χ = 2 to 2.2)	1 to 1.2	87
Damped flow	−0.06 to −0.11 (χ = 1.2 to 1.35)	0.25 to 0.4	33
Pulsed/damped ratio	2.2 to 3.9	2.5 to 4.5	2.6

f = 50 in both flow regimes.

Outlook for the implementation of pressure-pulsed flow for CO_2R

We note that our work is only a proof of concept for increasing the CO_2R rate with pressure-pulsed flow. Because the partial current density is still below that in gas-fed CO_2 electrolyzers, tuning the f, P_{PP}, and/or χ (using scaling relations in Equations 4 and 5), or increasing the CO_2 saturation pressure (which was currently dissolved at just 1 atm) would be next steps to meet industrial relevance. We suggest that a different pressure-pulse-generating system would allow us to operate at a lower flow rate (e.g., by creating the pressure oscillations with an additional piston instead of at the pump itself[40]).

To assess the potential for scaling and implementation of this technology, we consider three potential issues: (1) energy consumption of the pump; (2) contaminations and temperature effects due to the pump, and (3) damping of the pressure waves by gas bubbles upon scaling.

The compression of the electrolyzer during the pressure-pulsed flow requires energy. A calculation of the energy requirements, based on the thermodynamic work, is performed in Figure S14. The FE·VE of the pulsed system in Figure 3D would decrease from 30%–40% % to 22%–28%, when the compression energy is included into the voltage (see Figure S14). This decrease is more pronounced at lower current densities.

While the vibratory pump is effective at improving CO_2 mass transport, it has downsides as well. The flow rate of this pump is highly oversized for the electrode area (2 cm^2). Based on the solubility of CO_2 (33 mM at 25°C) and a partial CO-equiv current density of 87 mA/cm^2, we calculate that this flow rate provides more than 150× the required CO_2. Additionally, the electric energy consumption of the pump is relatively high (∼50 W), as coffee pumps are not designed for EE. The coil inside the pump produces a significant amount of heat, which increases the electrolyte temperature by 8°C–10°C over the course of the experiment. This higher temperature increases the ohmic resistance of the coil, which results in a lower P_{PP} and χ (see Figure S15) and reduces the CO_2 solubility, causing a 10%–30% lower $j_{CO\text{-}eq}$ after 35 min (see Figure S5). This could be a potential lever to decrease the energy consumption and remove the heating problem while maintaining high production rates.

Alternatively, the decrease in FE_{CO} over time (see Figure S5) can also be caused by contamination. We detected iron contamination on the electrode (20–40 ppm versus 5 ppm on electrodes with a stable FE_{CO}; see Figure S5), possibly polluted from the pump interior or impurities in the $KHCO_3$. This high sensitivity of the FE_{CO} to ppm levels of iron has also been observed by others.[7,8] The electrodes do not seem to be damaged by the pressure pulses, as the silver microstructures seem unchanged after 40 min of pulsation (see SEM images in Figure S17).

Finally, we considered the damping of pressure pulses during CO_2R experiments (Figure 5A), which is important for scaling up. Figure 5B shows pressure waves at 30 and 200 mA cm^{-2} at the inlet and outlet of the electrolyzer. We observed a reduction of P_{PP} and χ at the outlet, which was more pronounced at higher current densities. We define damping with Equation 6:

$$\text{Damping}\ (\%) = \frac{\chi_{\text{Inlet}} - \chi_{\text{Outlet}}}{\chi_{\text{Inlet}} - 1}. \qquad \text{(Equation 6)}$$

Here, χ_{Inlet} and χ_{Outlet} are the relative expansion at the inlet and outlet of the electrolyzer. The system fully damps the pressure pulses if χ_{Outlet} is 1. Figure 5C shows the effect of current density on damping. A steep increase in damping can be observed up to 90 mA cm^{-2}, after which the increase is more gradual. Because the damping increases with the current densities, we hypothesize that electrolytic gas bubbles inside the electrolyzer are the main cause of the damping. We expect the damping to increase for larger electrolyzers as there will be more gas bubbles in the system. The damping at the anode is stronger than at the cathode because of CO_2 bubbles are formed by recombination of H^+ and HCO_3^-, which makes the ratio of electrons to gas molecules at the anode and cathode 1.25 and 0.5, respectively. Unfortunately, damping reduces the effectiveness of the pressure pulses and therefore also reduces the mass transport. Thinner flow compartments with good bubble removal, which reduce the total gas-bubble volume, could mitigate this effect. Additionally, altering the interfacial conditions on the electrode could reduce damping and improve mass transport by influencing the bubble detachment dynamics.[57]

Conclusions

This work introduces a pressure-pulsed aqueous CO_2R electrolyzer. Using a cheap vibratory pump (∼18 euro), typically found in coffee machines, fast pressure pulses (50 Hz, 1–2.5 bar) were generated to improve the mass transport of dissolved CO_2 to the cathode. High current densities for CO_2R, up to 87 mA cm^{-2}, are obtained using a commercial silver mesh cathode, outperforming all H-cells in the literature and even most aqueous systems with elevated pressure. The limiting current density toward CO_2R products was 2.6 times higher compared to a system where the pressure waves were damped. Through a high-speed imaging analysis, PIV, and order-of-magnitude scaling, we identified that the enhanced mass transport is caused by oscillating gas bubbles and a multidirectional oscillatory flow.

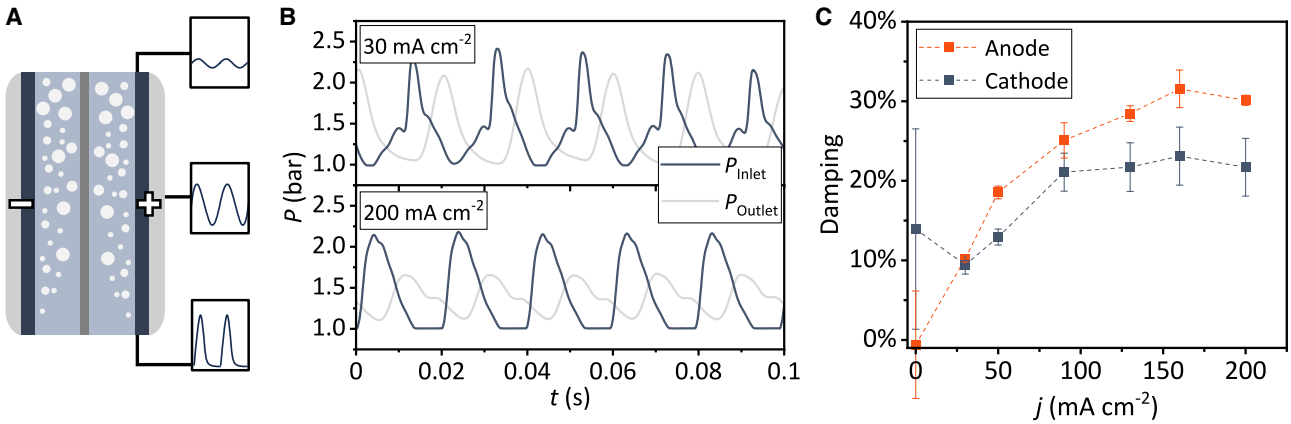

Figure 5. Pressure-wave damping analysis

(A) Graphical representation of pressure-wave damping through a CO_2R electrolyzer.

(B) Pressure waves at the inlet and outlet of the electrolyzer at 30 and 200 mA cm^{-2}.

(C) Time-averaged damping (Equation 6) versus current density. Damping is calculated over 40 min, where the first 5 min are skipped to ensure a steady gas-bubble state is achieved. The error bars indicate the standard deviation calculated for duplicate measurements.

Three potential engineering challenges were identified that could limit the implementation and scaling of this technology: (1) high energy consumption of the pump, (2) contaminations and temperature effects due to the pump, and (3) damping of the pressure waves by gas bubbles upon scaling.

On the other hand, the pressure-pulsed flow could be further leveraged by increasing the pressure-wave frequency (f), P_{PP}, and relative expansion (χ). Combining this optimization of the pumping parameters with using a more selective electrode and applying higher CO_2 concentrations (e.g., through supersaturated electrolytes), even higher limiting current densities could be achieved. Altogether, the pressure-pulsed concept is a promising new route for aqueous CO_2R.

METHODS

Pressure-pulsed CO_2R setup

The pressure-pulsed CO_2R setup consisted of a vibratory pump, an electrolyzer, a back-pressure regulator, and an electrolyte container with connections to a CO_2 gas bottle and gas chromatograph (GC) (see Figure 6A; for photos of the setup, see Figure S18). The vibratory pump (Ulka EP5) was controlled with a variable-frequency drive (VFD) (Schneider Electric ATV12H037M2). This VFD model requires three phases as output; therefore, we installed two other vibratory pumps that were circulating water in a separate reservoir. All three pumps were placed in a grounded aluminum box. During damped pressure-pulse experiments, we installed two pressure dampers (FPD 1.10 KPZ, KNF) between the pump and the electrolyzer inlet.

The electrolyzer consisted of two 3D printed poly(methyl methacrylate) (PMMA) backplates and two laser-cut, transparent, 4-mm thick PMMA flow channels (Figure 6B, drawings in Figure S18). A commercial silver mesh (80 woven, 0.115-mm diameter wire, 99.9% Thermo Scientific) was used as the cathode, and a titanium plate coated with mixed metal oxide (Ir/Ru, PSC-101 Permascand) was used as the anode. The two channels were separated with a Zirfon PERL UTP 500 separator. We used this porous diaphragm (instead of a commonly used anion-exchange membrane) for its good conductivity and mechanical strength, but recently it was even argued that porous separators feature more benefits in acidic CO_2 electrolyzers, such as decreased salt formation, low cost, and high FE.[58] To minimize pressure differences across the diaphragm, only one pump was used for both the anode and cathode compartment. Catholyte and anolyte were collected and mixed in the same electrolyte bottle. Silicone gaskets (thickness 0.5 mm) were used for sealing. Both the cathode and the anode have an exposed geometric electrode area of 2 cm^2 and were electrically connected to the potentiostat with silver wires (diameter 0.25 mm, 99.99%, Agosi). The electrolyzer was operated in a four-electrode configuration. An LF-1-45 leak-free Ag/AgCl (Innovative Instruments) was used as the reference electrode and a second silver wire connected to the cathode as the sense electrode. The cell was designed to handle pressures up to 7 bar.

The amplitude of the pressure pulses was controlled with a back-pressure regulator (Swagelok SS-1R4F) at the outlet of the cell. The pressure was recorded by four pressure transmitters (PT, TC Direct 716–908), which were connected to T junctions at the inlets and outlets of the electrolyzer. The temperature was measured by pressing thermocouples (K-type, TC Direct 405-011) against the tubing (see Figure 6A). The pressure transmitters and thermocouples were read with NI-9205 and NI-9213 modules at 5,000 and 1 Hz, respectively.

Experimental description

For each experiment, 200 mL of fresh liquid electrolyte (0.5 M $KHCO_3$, 99.5+%, Thermo Scientific) was continuously bubbled with 100 mL min^{-1} of CO_2 into the electrolyte container at atmospheric pressure. The gas headspace in the electrolyte container was 100 mL. Before starting the electrolysis, CO_2 was

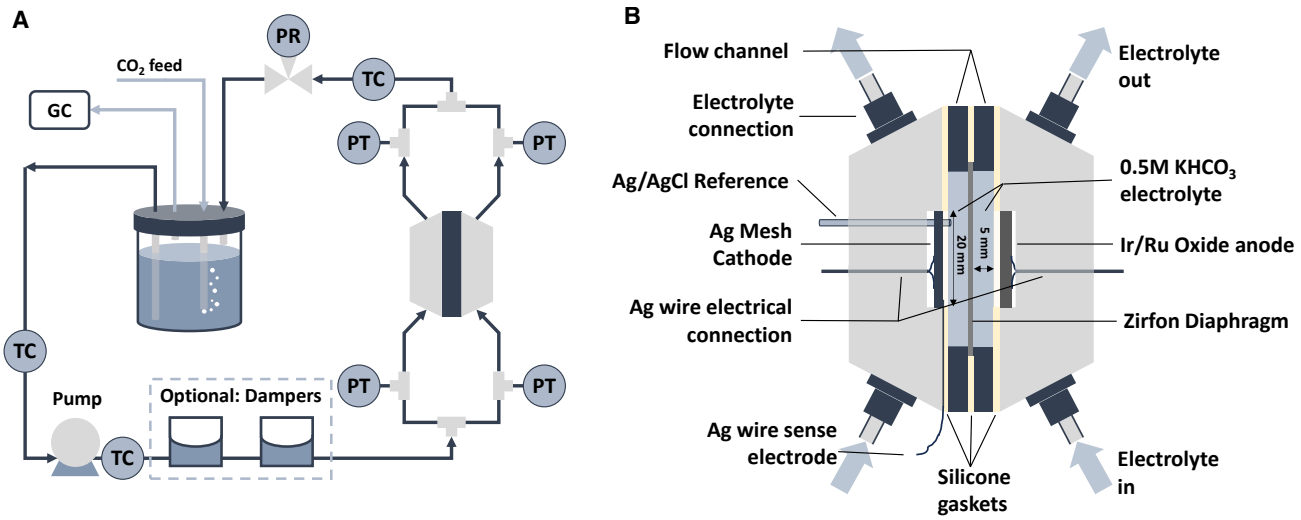

Figure 6. Schematic description of experimental setup

(A) Diagram of the pressure-pulsed CO_2-reduction setup. TC, thermocouple; PT, pressure transmitter; PR, back-pressure regulator; GC, gas chromatograph.
(B) Graphical representation of the CO_2 electrolyzer. See Figure S18 for a photo and a more detailed diagram of the electrolyzer.

pumped into the electrolyte for 15–20 min until the GC showed a CO_2 peak of >99%. The experiments were performed over ~40 min under constant current, controlled by an Ivium XP20 potentiostat. A GC sample was taken from the electrolyte container headspace every 3.5 min (Compact GC4.0, Interscience). The methods and setup of Baumgartner et al.[17] were used to calculate the FE of gas products. A liquid sample was taken at the end of the experiment and analyzed with high-performance liquid chromatography (HPLC) (1290 Infinity II, Agilent) according to the methods of Kortlever et al.[32] The FE of liquid products was assumed constant over an experiment, due to lack of time-resolved data. The starting temperature of the electrolyte was between 18°C and 22°C. The pump generated a significant amount of heat, which caused the temperature to increase by 8°C–10°C over the 40 min. The electrolyte container was placed in an ice bucket to limit the temperature to 35°C.

Electrode pre-treatment and SEM analysis

Before each experiment, a fresh cathode was cleaned by holding it in a propane flame. The cathode was then placed inside the cell and anodized for 1 min by applying a current density of 10 mA cm^{-2}. After flushing the cell with fresh electrolyte, the experiment was started, leading to a reduction of the oxidized silver surface and resulting in a roughening of the silver surface (Figure S19). The pre-treatment of the cathode with a constant anodizing current almost doubled the FE toward CO and increased the catalyst stability over time (Figure S19).

High-speed imaging

High-speed imaging and PIV were used to investigate the mixing phenomena and velocity fields inside the electrolyzer. To make the channel more transparent, a glass microscope slide was glued to the outside of the channel with Araldite 2020. A LaVision Imager HS 4M camera was used for imaging at a rate of 3.7 kHz. The electrolyte used during the PIV measurements was demineralized water seeded with 4-μm tracer particles (PS-FluoRed-Fi191, microParticles GmbH). For a detailed description of the imaging setup and method see Figure S7.

RESOURCE AVAILABILITY

Lead contact

Further information and requests should be directed to David Vermaas (d.a.vermaas@tudelft.nl).

Materials availability

This study did not generate new unique materials.

Data and code availability

- The data supporting the findings of this study are contained within the paper and its associated supplemental information.
- All other relevant data are available from the corresponding author upon reasonable request and in the Zenodo repository at https://zenodo.org/records/14018473.

ACKNOWLEDGMENTS

This project has received funding from the Horizon 2020 European Research Council (grant agreement no. 852115). This work reflects the authors' views, and the ERC Executive Agency is not responsible for any use resulting from the information it contains. The authors thank Kevin Kamman and Stefan ten Hagen (TU Delft) for their technical support, and Christel Koopman, Ruud Kortlever, Valeria Garbin, Vojtech Konderla, and Yu-Fan Lee (TU Delft) for the insightful discussions.

AUTHOR CONTRIBUTIONS

Conceptualization, J.B. and D.A.V.; formal analysis, J.B., L.C.B., S.S.J.v.D., T.J.J.M.v.O., and G.L.; investigation, J.B., L.C.B., S.S.J.v.D., K.M.R.L., C.V.S., and E.C.W.; methodology, J.B., L.C.B., S.S.J.v.D., I.B., D.B., and D.A.V.; supervision, J.R.v.O., and D.A.V.; writing – original draft, J.B.; writing – review & editing, J.B., L.C.B., S.S.J.v.D., T.J.J.M.v.O., K.M.R.L., I.B., G.L., J.R.v.O., and D.A.V.; funding acquisition, D.A.V.

DECLARATION OF INTERESTS

The authors declare no competing interests.

SUPPLEMENTAL INFORMATION

Supplemental information can be found online at https://doi.org/10.1016/j.checat.2025.101547.

Received: May 24, 2025
Revised: July 15, 2025
Accepted: September 16, 2025
Published: October 16, 2025

REFERENCES

1. Smith, W.A., Burdyny, T., Vermaas, D.A., and Geerlings, H. (2019). Pathways to industrial-scale fuel out of thin air from CO2 electrolysis. Joule *3*, 1822–1834.
2. Li, M., Yang, K., Abdinejad, M., Zhao, C., and Burdyny, T. (2022). Advancing integrated CO2 electrochemical conversion with amine-based CO2 capture: a review. Nanoscale *14*, 11892–11908. https://doi.org/10.1039/D2NR03310K.
3. Endrődi, B., Bencsik, G., Darvas, F., Jones, R., Rajeshwar, K., and Janáky, C. (2017). Continuous-flow electroreduction of carbon dioxide. Prog. Energy Combust. Sci. *62*, 133–154. https://doi.org/10.1016/j.pecs.2017.05.005.
4. Hori, Y. (2008). Electrochemical CO2 Reduction on Metal Electrodes. In Modern Aspects of Electrochemistry, C.G. Vayenas, R.E. White, and M.E. Gamboa-Aldeco, eds. (Springer), pp. 89–189. https://doi.org/10.1007/978-0-387-49489-0_3.
5. Zhang, B.A., Costentin, C., and Nocera, D.G. (2019). On the Conversion Efficiency of CO2 Electroreduction on Gold. Joule *3*, 1565–1568. https://doi.org/10.1016/j.joule.2019.05.017.
6. Burdyny, T., Graham, P.J., Pang, Y., Dinh, C.-T., Liu, M., Sargent, E.H., and Sinton, D. (2017). Nanomorphology-Enhanced Gas-Evolution Intensifies CO2 Reduction Electrochemistry. ACS Sustain. Chem. Eng. *5*, 4031–4040. https://doi.org/10.1021/acssuschemeng.7b00023.
7. Staerz, A.F., van Leeuwen, M., Priamushko, T., Saatkamp, T., Endrődi, B., Plankensteiner, N., Jobbagy, M., Pahlavan, S., Blom, M.J.W., Janáky, C., et al. (2024). Effects of Iron Species on Low Temperature CO2 Electrolyzers. Angew Chem. Int. Ed. Engl. *63*, e202306503. https://doi.org/10.1002/anie.202306503.
8. Obasanjo, C.A., Gao, G., Crane, J., Golovanova, V., García de Arquer, F.P., and Dinh, C.-T. (2023). High-rate and selective conversion of CO2 from aqueous solutions to hydrocarbons. Nat. Commun. *14*, 3176.
9. Chen, C., Li, Y., Yu, S., Louisia, S., Jin, J., Li, M., Ross, M.B., and Yang, P. (2020). Cu-Ag Tandem Catalysts for High-Rate CO2 Electrolysis toward Multicarbons. Joule *4*, 1688–1699. https://doi.org/10.1016/j.joule.2020.07.009.
10. Tan, Y.C., Lee, K.B., Song, H., and Oh, J. (2020). Modulating Local CO2 Concentration as a General Strategy for Enhancing C–C Coupling in CO2 Electroreduction. Joule *4*, 1104–1120. https://doi.org/10.1016/j.joule.2020.03.013.
11. Iglesias van Montfort, H.-P., Subramanian, S., Irtem, E., Sassenburg, M., Li, M., Kok, J., Middelkoop, J., and Burdyny, T. (2023). An Advanced Guide to Assembly and Operation of CO2 Electrolyzers. ACS Energy Lett. *8*, 4156–4161. https://doi.org/10.1021/acsenergylett.3c01561.
12. Gabardo, C.M., O'Brien, C.P., Edwards, J.P., McCallum, C., Xu, Y., Dinh, C.-T., Li, J., Sargent, E.H., and Sinton, D. (2019). Continuous Carbon Dioxide Electroreduction to Concentrated Multi-carbon Products Using a Membrane Electrode Assembly. Joule *3*, 2777–2791. https://doi.org/10.1016/j.joule.2019.07.021.
13. Raya-Imbernón, A., Samu, A.A., Barwe, S., Cusati, G., Fődi, T., Hepp, B.M., and Janáky, C. (2024). Renewable Syngas Generation via Low-Temperature Electrolysis: Opportunities and Challenges. ACS Energy Lett. *9*, 288–297. https://doi.org/10.1021/acsenergylett.3c02446.
14. She, X., Zhai, L., Wang, Y., Xiong, P., Li, M.M.-J., Wu, T.-S., Wong, M.C., Guo, X., Xu, Z., Li, H., et al. (2024). Pure-water-fed, electrocatalytic CO2 reduction to ethylene beyond 1,000 h stability at 10 A. Nat. Energy *9*, 81–91. https://doi.org/10.1038/s41560-023-01415-4.
15. Baumgartner, L.M., Goryachev, A., Koopman, C.I., Franzen, D., Ellendorff, B., Turek, T., and Vermaas, D.A. (2023). Electrowetting limits electrochemical CO2 reduction in carbon-free gas diffusion electrodes. Energy Adv. *2*, 1893–1904. https://doi.org/10.1039/D3YA00285C.
16. Hoof, L., Thissen, N., Pellumbi, K., junge Puring, K., Siegmund, D., Mechler, A.K., and Apfel, U.-P. (2022). Hidden parameters for electrochemical carbon dioxide reduction in zero-gap electrolyzers. Cell Rep. Phys. Sci. *3*, 100825. https://doi.org/10.1016/j.xcrp.2022.100825.
17. Baumgartner, L.M., Koopman, C.I., Forner-Cuenca, A., and Vermaas, D.A. (2022). Narrow Pressure Stability Window of Gas Diffusion Electrodes Limits the Scale-Up of CO2 Electrolyzers. ACS Sustain. Chem. Eng. *10*, 4683–4693. https://doi.org/10.1021/acssuschemeng.2c00195.
18. Yang, K., Kas, R., Smith, W.A., and Burdyny, T. (2021). Role of the Carbon-Based Gas Diffusion Layer on Flooding in a Gas Diffusion Electrode Cell for Electrochemical CO2 Reduction. ACS Energy Lett. *6*, 33–40. https://doi.org/10.1021/acsenergylett.0c02184.
19. Sassenburg, M., Kelly, M., Subramanian, S., Smith, W.A., and Burdyny, T. (2023). Zero-Gap Electrochemical CO2 Reduction Cells: Challenges and Operational Strategies for Prevention of Salt Precipitation. ACS Energy Lett. *8*, 321–331. https://doi.org/10.1021/acsenergylett.2c01885.
20. Keith, D.W., Holmes, G., St. Angelo, D., and Heidel, K. (2018). A Process for Capturing CO2 from the Atmosphere. Joule *2*, 1573–1594. https://doi.org/10.1016/j.joule.2018.05.006.
21. Sabatino, F., Grimm, A., Gallucci, F., van Sint Annaland, M., Kramer, G.J., and Gazzani, M. (2021). A comparative energy and costs assessment and optimization for direct air capture technologies. Joule *5*, 2047–2076. https://doi.org/10.1016/j.joule.2021.05.023.
22. Pérez-Gallent, E., Vankani, C., Sánchez-Martínez, C., Anastasopol, A., and Goetheer, E. (2021). Integrating CO2 Capture with Electrochemical Conversion Using Amine-Based Capture Solvents as Electrolytes. Ind. Eng. Chem. Res. *60*, 4269–4278. https://doi.org/10.1021/acs.iecr.0c05848.
23. Li, M., Irtem, E., Iglesias van Montfort, H.-P., Abdinejad, M., and Burdyny, T. (2022). Energy comparison of sequential and integrated CO2 capture and electrochemical conversion. Nat. Commun. *13*, 5398. https://doi.org/10.1038/s41467-022-33145-8.
24. Almajed, H.M., Kas, R., Brimley, P., Crow, A.M., Somoza-Tornos, A., Hodge, B.-M., Burdyny, T.E., and Smith, W.A. (2024). Closing the Loop: Unexamined Performance Trade-Offs of Integrating Direct Air Capture with (Bi)carbonate Electrolysis. ACS Energy Lett. *9*, 2472–2483. https://doi.org/10.1021/acsenergylett.4c00807.
25. Lee, M.-Y., Park, K.T., Lee, W., Lim, H., Kwon, Y., and Kang, S. (2020). Current achievements and the future direction of electrochemical CO2 reduction: A short review. Crit. Rev. Environ. Sci. Technol. *50*, 769–815. https://doi.org/10.1080/10643389.2019.1631991.
26. Morrison, A.R.T., Girichandran, N., Wols, Q., and Kortlever, R. (2023). Design of an elevated pressure electrochemical flow cell for CO2 reduction. J. Appl. Electrochem. *53*, 2321–2330.
27. Ramdin, M., Morrison, A.R.T., de Groen, M., van Haperen, R., de Kler, R., van den Broeke, L.J.P., Trusler, J.P.M., de Jong, W., and Vlugt, T.J.H. (2019). High Pressure Electrochemical Reduction of CO2 to Formic Acid/Formate: A Comparison between Bipolar Membranes and Cation Exchange Membranes. Ind. Eng. Chem. Res. *58*, 1834–1847. https://doi.org/10.1021/acs.iecr.8b04944.
28. Hashiba, H., Yotsuhashi, S., Deguchi, M., and Yamada, Y. (2016). Systematic Analysis of Electrochemical CO2 Reduction with Various Reaction Parameters using Combinatorial Reactors. ACS Comb. Sci. *18*, 203–208. https://doi.org/10.1021/acscombsci.6b00021.

29. Qi, K., Zhang, Y., Onofrio, N., Petit, E., Cui, X., Ma, J., Fan, J., Wu, H., Wang, W., Li, J., et al. (2023). Unlocking direct CO2 electrolysis to C3 products via electrolyte supersaturation. Nat. Catal. *6*, 319–331. https://doi.org/10.1038/s41929-023-00938-z.

30. Abdinejad, M., Mirza, Z., Zhang, X.-a., and Kraatz, H.-B. (2020). Enhanced Electrocatalytic Activity of Primary Amines for CO2 Reduction Using Copper Electrodes in Aqueous Solution. ACS Sustain. Chem. Eng. *8*, 1715–1720. https://doi.org/10.1021/acssuschemeng.9b06837.

31. Sullivan, I., Goryachev, A., Digdaya, I.A., Li, X., Atwater, H.A., Vermaas, D.A., and Xiang, C. (2021). Coupling electrochemical CO2 conversion with CO2 capture. Nat. Catal. *4*, 952–958. https://doi.org/10.1038/s41929-021-00699-7.

32. Burgers, I., Pérez-Gallent, E., Goetheer, E., and Kortlever, R. (2023). Electrochemical CO2 Reduction on Copper in Propylene Carbonate: Influence of Water Content and Temperature on the Product Distribution. Energ. Tech. *11*, 2201465. https://doi.org/10.1002/ente.202201465.

33. Kumar, A.S., Pupo, M., Petrov, K.V., Ramdin, M., van Ommen, J.R., de Jong, W., and Kortlever, R. (2023). A Quantitative Analysis of Electrochemical CO2 Reduction on Copper in Organic Amide and Nitrile-Based Electrolytes. J. Phys. Chem. C Nanomater. Interfaces *127*, 12857–12866. https://doi.org/10.1021/acs.jpcc.3c01955.

34. Masel, R.I., Liu, Z., Yang, H., Kaczur, J.J., Carrillo, D., Ren, S., Salvatore, D., and Berlinguette, C.P. (2021). An industrial perspective on catalysts for low-temperature CO2 electrolysis. Nat. Nanotechnol. *16*, 118–128. https://doi.org/10.1038/s41565-020-00823-x.

35. Liu, M., Pang, Y., Zhang, B., De Luna, P., Voznyy, O., Xu, J., Zheng, X., Dinh, C.T., Fan, F., Cao, C., et al. (2016). Enhanced electrocatalytic CO2 reduction via field-induced reagent concentration. Nature *537*, 382–386. https://doi.org/10.1038/nature19060.

36. Nesbitt, N.T., Ma, M., Trześniewski, B.J., Jaszewski, S., Tafti, F., Burns, M.J., Smith, W.A., and Naughton, M.J. (2018). Au Dendrite Electrocatalysts for CO2 Electrolysis. J. Phys. Chem. C *122*, 10006–10016. https://doi.org/10.1021/acs.jpcc.8b01831.

37. Bagemihl, I., Bhatraju, C., van Ommen, J.R., and van Steijn, V. (2022). Electrochemical Reduction of CO2 in Tubular Flow Cells under Gas–Liquid Taylor Flow. ACS Sustain. Chem. Eng. *10*, 12580–12587. https://doi.org/10.1021/acssuschemeng.2c03038.

38. Wen, G., Ren, B., Wang, X., Luo, D., Dou, H., Zheng, Y., Gao, R., Gostick, J., Yu, A., and Chen, Z. (2022). Continuous CO2 electrolysis using a CO2 exsolution-induced flow cell. Nat. Energy *7*, 978–988. https://doi.org/10.1038/s41560-022-01130-6.

39. Pérez-Gallent, E., Sánchez-Martínez, C., Geers, L.F.G., Turk, S., Latsuzbaia, R., and Goetheer, E.L.V. (2020). Overcoming Mass Transport Limitations in Electrochemical Reactors with a Pulsating Flow Electrolyzer. Ind. Eng. Chem. Res. *59*, 5648–5656. https://doi.org/10.1021/acs.iecr.9b06925.

40. Saremirad, P., Gomaa, H.G., and Zhu, J. (2012). Effect of flow oscillations on mass transfer in electrodialysis with bipolar membrane. J. Membr. Sci. *405–406*, 158–166. https://doi.org/10.1016/j.memsci.2012.03.006.

41. De Wolf, R., Rossen, A., De Rop, M., Arenas, L.F., Breugelmans, T., and Hereijgers, J. (2024). Improved Vanadium Flow Battery Performance through a Pulsating Electrolyte Flow Regime. Batter. Supercaps *7*, e202300382. https://doi.org/10.1002/batt.202300382.

42. Vranckaert, M., Gemoets, H.P.L., Dangreau, R., Van Aken, K., Breugelmans, T., and Hereijgers, J. (2022). An electrochemical oscillatory flow reactor with pillar array electrodes improving mass transfer in electrosynthesis. Electrochim. Acta *436*, 141435. https://doi.org/10.1016/j.electacta.2022.141435.

43. Rossi, L., and Crotti, R. (1980) Alternating Action Electromagnetic Piston Pump - Has Magnetic Piston Acting against Spring in Body Surrounded by Excitation Coil Housed within Cylindrical Shell. (FR2465903A1).

44. Hatsukade, T., Kuhl, K.P., Cave, E.R., Abram, D.N., and Jaramillo, T.F. (2014). Insights into the electrocatalytic reduction of CO 2 on metallic silver surfaces. Phys. Chem. Chem. Phys. *16*, 13814–13819.

45. Kauffman, D.R., Alfonso, D., Matranga, C., Qian, H., and Jin, R. (2012). Experimental and computational investigation of Au25 clusters and CO2: a unique interaction and enhanced electrocatalytic activity. J. Am. Chem. Soc. *134*, 10237–10243.

46. Lu, Q., Rosen, J., Zhou, Y., Hutchings, G.S., Kimmel, Y.C., Chen, J.G., and Jiao, F. (2014). A selective and efficient electrocatalyst for carbon dioxide reduction. Nat. Commun. *5*, 3242. https://doi.org/10.1038/ncomms4242.

47. Ma, M., Trześniewski, B.J., Xie, J., and Smith, W.A. (2016). Selective and efficient reduction of carbon dioxide to carbon monoxide on oxide-derived nanostructured silver electrocatalysts. Angew. Chem. *128*, 9900–9904.

48. Lamaison, S., Wakerley, D., Blanchard, J., Montero, D., Rousse, G., Mercier, D., Marcus, P., Taverna, D., Giaume, D., Mougel, V., and Fontecave, M. (2020). High-current-density CO2-to-CO electroreduction on Ag-alloyed Zn dendrites at elevated pressure. Joule *4*, 395–406.

49. Clark, E.L., Resasco, J., Landers, A., Lin, J., Chung, L.-T., Walton, A., Hahn, C., Jaramillo, T.F., and Bell, A.T. (2018). Standards and protocols for data acquisition and reporting for studies of the electrochemical reduction of carbon dioxide. ACS Catal. *8*, 6560–6570.

50. Zhou, Y., Che, F., Liu, M., Zou, C., Liang, Z., De Luna, P., Yuan, H., Li, J., Wang, Z., Xie, H., et al. (2018). Dopant-induced electron localization drives CO2 reduction to C2 hydrocarbons. Nat. Chem. *10*, 974–980. https://doi.org/10.1038/s41557-018-0092-x.

51. Lee, G., Rasouli, A.S., Lee, B.-H., Zhang, J., Won, D.H., Xiao, Y.C., Edwards, J.P., Lee, M.G., Jung, E.D., Arabyarmohammadi, F., et al. (2023). CO2 electroreduction to multicarbon products from carbonate capture liquid. Joule *7*, 1277–1288. https://doi.org/10.1016/j.joule.2023.05.003.

52. Li, Y.C., Lee, G., Yuan, T., Wang, Y., Nam, D.-H., Wang, Z., García de Arquer, F.P., Lum, Y., Dinh, C.-T., Voznyy, O., and Sargent, E.H. (2019). CO2 Electroreduction from Carbonate Electrolyte. ACS Energy Lett. *4*, 1427–1431. https://doi.org/10.1021/acsenergylett.9b00975.

53. Lees, E.W., Goldman, M., Fink, A.G., Dvorak, D.J., Salvatore, D.A., Zhang, Z., Loo, N.W.X., and Berlinguette, C.P. (2020). Electrodes Designed for Converting Bicarbonate into CO. ACS Energy Lett. *5*, 2165–2173. https://doi.org/10.1021/acsenergylett.0c00898.

54. Zhang, Z., Lees, E.W., Habibzadeh, F., Salvatore, D.A., Ren, S., Simpson, G.L., Wheeler, D.G., Liu, A., and Berlinguette, C.P. (2022). Porous metal electrodes enable efficient electrolysis of carbon capture solutions. Energy Environ. Sci. *15*, 705–713. https://doi.org/10.1039/D1EE02608A.

55. Haynes, W.M. (2014). CRC Handbook of Chemistry and Physics, 95th Edition. 95th ed ed. (CRC Press).

56. Zhao, X., Ren, H., and Luo, L. (2019). Gas Bubbles in Electrochemical Gas Evolution Reactions. Langmuir *35*, 5392–5408. https://doi.org/10.1021/acs.langmuir.9b00119.

57. Kempler, P.A., Coridan, R.H., and Luo, L. (2024). Gas Evolution in Water Electrolysis. Chem. Rev. *124*, 10964–11007. https://doi.org/10.1021/acs.chemrev.4c00211.

58. Ha, T.H., Kim, J., Choi, H., and Oh, J. (2024). Selective Zero-Gap CO2 Reduction in Acid. ACS Energy Lett. *9*, 4835–4842. https://doi.org/10.1021/acsenergylett.4c01410.